nature catalysis

SUPPLEMENTARY INFORMATION

https://doi.org/10.1038/s41929-017-0018-9

In the format provided by the authors and unedited.

Catalyst electro-redeposition controls morphology and oxidation state for selective carbon dioxide reduction

Phil De Luna[1,2,3], Rafael Quintero-Bermudez[4], Cao-Thang Dinh[4], Michael B. Ross[2,3], Oleksandr S. Bushuyev[4], Petar Todorović[4], Tom Regier[5], Shana O. Kelley[6,7], Peidong Yang[2,3,8,9,10,11] and Edward H. Sargent[2,4]*

[1]Department of Materials Science and Engineering, University of Toronto, Toronto, ON, Canada. [2]Bio-inspired Solar Energy Program, Canadian Institute for Advanced Research, Toronto, ON, Canada. [3]Department of Chemistry, University of California, Berkeley, Berkeley, CA, USA. [4]Department of Electrical and Computer Engineering, University of Toronto, Toronto, ON, Canada. [5]Canadian Light Source Inc. (CLSI), Saskatoon, SK, Canada. [6]Department of Pharmaceutical Sciences, Leslie Dan Faculty of Pharmacy, University of Toronto, Toronto, ON, Canada. [7]Department of Biochemistry, Faculty of Medicine, University of Toronto, Toronto, ON, Canada. [8]Department of Materials Science and Engineering, University of California, Berkeley, Berkeley, CA, USA. [9]Materials Sciences Division, Lawrence Berkeley National Laboratory, Berkeley, CA, USA. [10]Chemical Sciences Division, Lawrence Berkeley National Laboratory, Berkeley, CA, USA. [11]Kavli Energy Nanosciences Institute, University of California, Berkeley, Berkeley, CA, USA. Phil De Luna and Rafael Quintero-Bermudez contributed equally to this work. *e-mail: ted.sargent@utoronto.ca

Supplementary Methods

Computational Details

All density functional theory (DFT) calculations were carried out with the Vienna Ab Initio Simulation package (VASP)[1]. The projector augmented wave (PAW) method[2] was used with the Perdew-Burke-Ernzerhof (PBE)[3] generalized gradient approximation (GGA) exchange correlation functional. All-electron frozen-core PAW pseudopotentials with a plane wave basis set as described by Blöchl[4] were used with a cutoff energy of 500 eV, and fermi smearing width of 0.1 eV and dipole corrections were employed. Monkhorst-Pack mesh[5] was used for k-point sampling with 6x6x6 k-points sampled for the optimization of all bulk structures and 5x5x1 k-points sampled for all vacuum slabs of Cu and Cu/Cu_2O. The {111} and {211} facets were used with a 4x4x4 atom slab and 20Å between mirror images in the z-axis in the unit cell. Structural and unit cell optimizations were performed with the Broyden-Fletcher-Goldfarb-Shanno (BFGS)[6] algorithm until the maximum cutoff was less than 0.02 eV/atom with the structures being fully optimized. Once the slab models were optimized all subsequent thermodynamic calculations were performed with the bottom two layers fixed.

For the calculation of all thermodynamic quantities, the open-source atomic simulation environment (ASE)[7] code was used. The Gibbs free energies were calculated at 298K and 1 atm as outlined below:

$$G = H - TS = E_{DFT} + E_{ZPE} + \int_0^{298} C_v dT - TS \qquad (1)$$

where E_{DFT} is the DFT calculated electronic energy, E_{ZPE} is the zero-point vibrational energy, $\int_0^{298} C_v dT$ is the heat capacity, T is the temperature, and S is the entropy. Gas phase molecules such as CO_2 and H_2 were treated using the ideal gas approximation while adsorbates were treated using a harmonic approximation. The computational hydrogen electrode model (CHE)[8] was used to calculate the Gibbs free

formation energy for methane and ethylene intermediates COH* and OCCOH*. The Gibbs free energy of formation for OCCOH* is calculated as $G_{Form}(OCCOH^*) = G_{OCCOH^*} - (G_{CO^*+CO^*} + G_{H2}/2)$. The Gibbs free energy of formation for COH* is calculated as $G_{Form}(COH) = G_{COH^*} - (G_{CO^*} + G_{H2}/2)$. The binding energy of CO is calculated as $E_{bind}(CO) = E_{CO^*} - (E_{slab} + E_{co})$.

Chemicals

Copper (II) chloride dihydrate (99.999%, CAS 10125-13-0), copper powder (99.999% trace metal basis, CAS 7440-50-8), copper (II) oxide powder (CAS 1317-38-0), copper (I) oxide power (99.99% CAS 1317-39-1), (±)-Propylene oxide (ReagentPlus®, >99%, CAS 75-56-9), and ~5% Nafion 117 solution (CAS 31175-20-9) were purchased from Sigma-Aldrich. Toray TGP-H-060 carbon paper was purchased from Fuel Cell Store.

Experimental Synthesis

In a typical synthesis, 3 mmol of copper (II) chloride dihydrate (Sigma-Aldrich) is dissolved in 2 mL 2-proponal (Sigma-Aldrich, anhydrous, 99.5%) to yield a transparent green solution. Next, 2 mL of epoxide (Sigma Aldrich, (±)-Propylene oxide ReagentPlus®, 99%) and 0.2 mL of deionized water were slowly added with under constant stirring resulting in a blue solution. The solution was then allowed to age in room temperature for >24 hours to promote network formation and gelation. After aging, the gels were repeatedly washed and centrifuged with acetone (3 x 15 mL) to remove any 2-propanol and then dried under vacuum for 24 hours. The resulting sol-gel was then ground into a fine powder using a mortar and pestle. To prepare the deposition ink 10 mg of this powder was dispersed in a mixture of 0.5 mL ethanol, 0.5 mL water, and 50 µL 5% Nafion 117 solution (Sigma-Aldrich) and then sonicated for at least 30 minutes. The ink was air-brushed onto 0.25 cm^2 carbon paper (Toray TGP-H-060, purchased from Fuel Cell Store) with a loading of 0.65 mg/cm^2 and dried to form the copper sol-gel working electrode. The loading was determined by measuring the weight of the carbon paper before and after deposition. The active catalyst

was then formed by reduction at specific applied potential in CO_2 saturated 0.1 M $KHCO_3$ electrolyte (pH 7.2). The colour of the catalyst began to change from blue to black within 5 minutes and was completely black by 10 minutes regardless of potential applied, resulting in the active SGD-Cu catalyst. The copper nanoneedle catalysts (NN-Cu) were electrodeposited on carbon paper from a deposition solution of 0.15 M $CuCl_2$ in 0.5 M HCl using an applied potential of -0.7 V vs. Ag/AgCl for 1000s.

Supplementary Discussion

Faradaic efficiency and nanostructured growth:

To provide better correlation between the product distribution and the growth of sharp nanostructured morphologies, we have measured the FE of major gas products as a function of time over 1 hour of operation at -1.2 V vs. RHE (**Figure S16**). As it has been shown that the nanostructured morphologies grow with respect to time over the first 20 minutes, one would expect the product distribution to also change over the first 20 minutes. The first measurement at 5 minutes was taken in a closed cell configuration with CO_2 saturated 0.1 M KHCO3 electrolyte as a batch measurement to ensure all product was only from catalytic activity. The measurements at 10, 20, 40 and 60 mins were performed with CO_2 bubbling through the catholyte. It was found that in the first 5 minutes, the majority product is hydrogen with a FE_{C2H4} of 15%. However, at 10 minutes the FE_{H2} has stabilized at 30% and remains at approximately 30% throughout the reaction. The FE_{C2H4} continues to increase with respect to time and by 40 mins it has reached its maximum FE of ~39%. The FE_{CH4} remained consistently below 1%. The time resolved FE data shows that in the beginning there is a high amount of Cu^+, but a low amount of sharp nanostructures. This means the local pH is not high and thus HER dominates the reaction. As time continues the sharper nanostructures start to grow, leading to high pH, suppressing HER. While the amount of Cu^+ decreases, the system reaches an equilibrium where there is a large interface of Cu^+ and

Cu^0 which has been shown to favour ethylene.[9] These results suggest that the oxidation state primarily promotes ethylene production, which is in agreement with DFT results.

Flowcell stability: The electrocatalytic performance of ERD-Cu was determined in a flowcell configuration similar to those previously published.[10] This setup consists of ERD-Cu spray-coated on a Freudenberg gas diffusion layer (GDL), anion exchange membrane, and nickel mesh as the anode. The GDL, anion exchange membrane, and anode were assembled using PTFE spacers with liquid electrolyte flowing (10mL per min) in the chambers between anode and membrane and membrane and cathode. CO_2 gas was flowed behind the gas diffusion layer at a rate of 50 mL per min. Chronopotentiometry experiments were performed at a fixed current of -0.5 A, -0.75 A, and -1 A (**Figure S3a**) showing consistent gas product distributions.

Over an hour of operation, the potential of the system was constant, showing good electrochemical stability (**Figure S3b**). However, after an hour of operation the FE_{C2H4} decreased to 25.5% while the FE_{H2} increased to 21.7%. This decrease in ethylene production can be explained by the amount of severe cracks in the catalyst GDL electrode (**Figure S3c**). Over time, the high current densities result in large bubble generation which leads to cracks in the catalyst film, exposing the underlying carbon paper substrate. This results in hydrogen generation coming primarily from the exposed carbon and thus a decrease in ethylene FE. The sharp nanostructures found in the H-cell configuration was present and consistent on ERD-Cu in flow cell (**Figure S3d**).

X-ray absorption spectroscopy:

hXAS measurements at the Cu K-edge probe high-energy transitions between 1s and 4p electronic orbitals and are prevalent and can be used as a probe of local coordination environment. However, hXAS weakly captures 3d final states (a descriptor for catalytic activity)[11] as 1s to 3d excitation is dipole-forbidden. As a result, the 3d electron configuration is only faintly present in hXAS as low-intensity pre-edge features that occur due to low probability quadrupole transitions.[12] Thus, hXAS pre-edges do not

provide a robust determination of the narrow band transition metal 3d electronic structure. In contrast, sXAS directly measures the lower energy transition of a metal 2p electron to the 3d state and is electric-dipole allowed giving a more intense signal than the metal K pre-edge.

Supplementary Figures

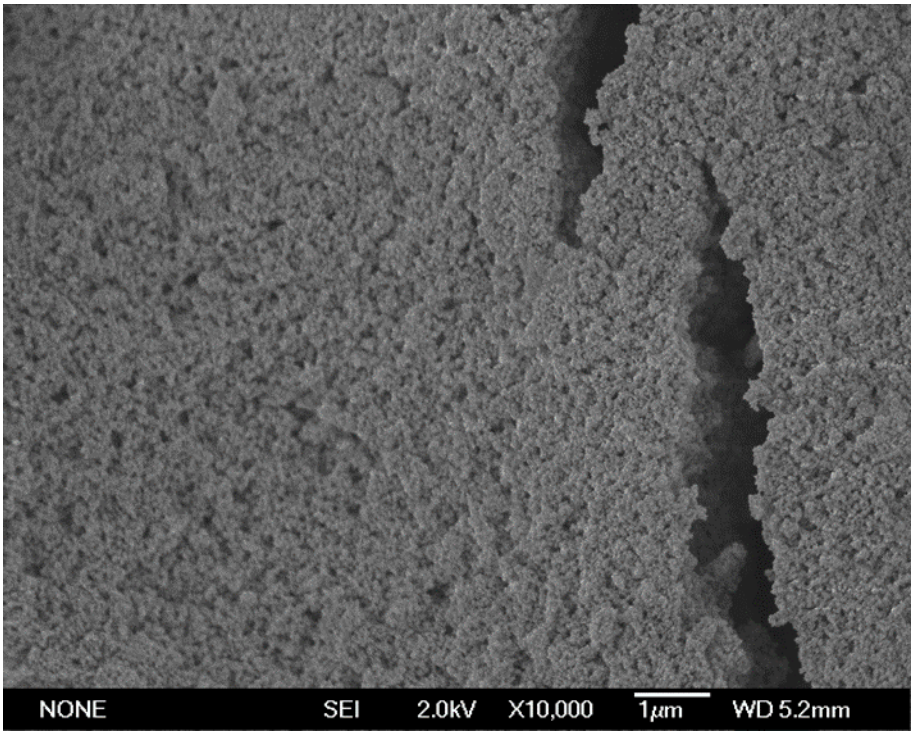

Supplementary Figure 1. SEM image of porous deposited copper oxychloride on carbon paper.

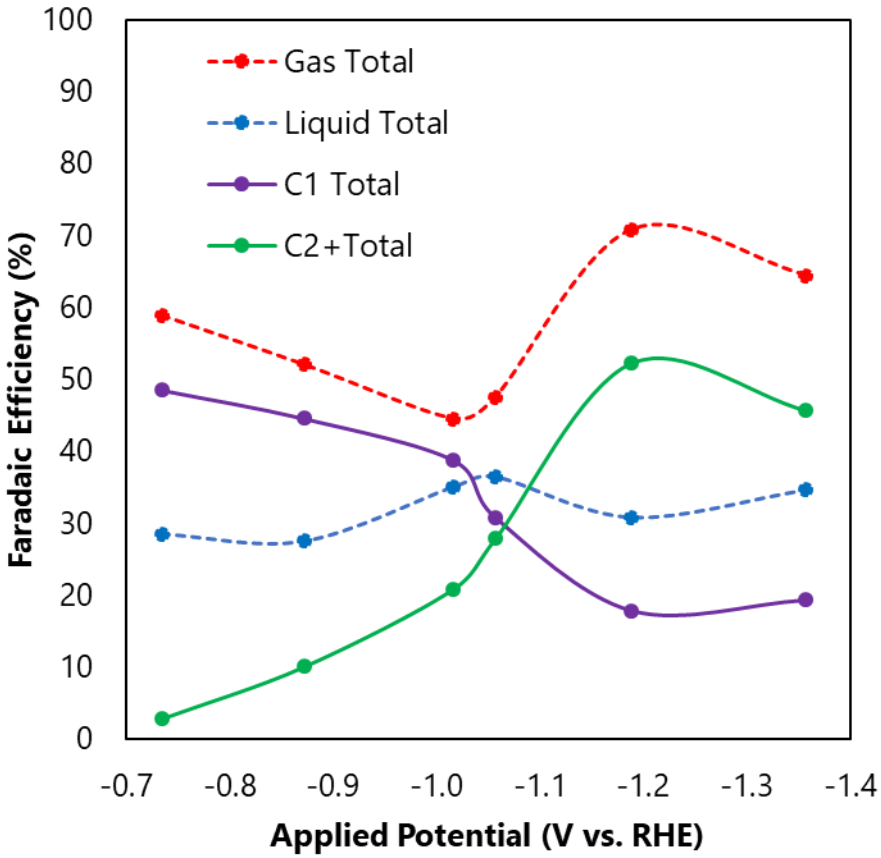

Supplementary Figure 2. Faradaic efficiencies categorized as C1, C2+, liquid, and gas products for ERD-Cu.

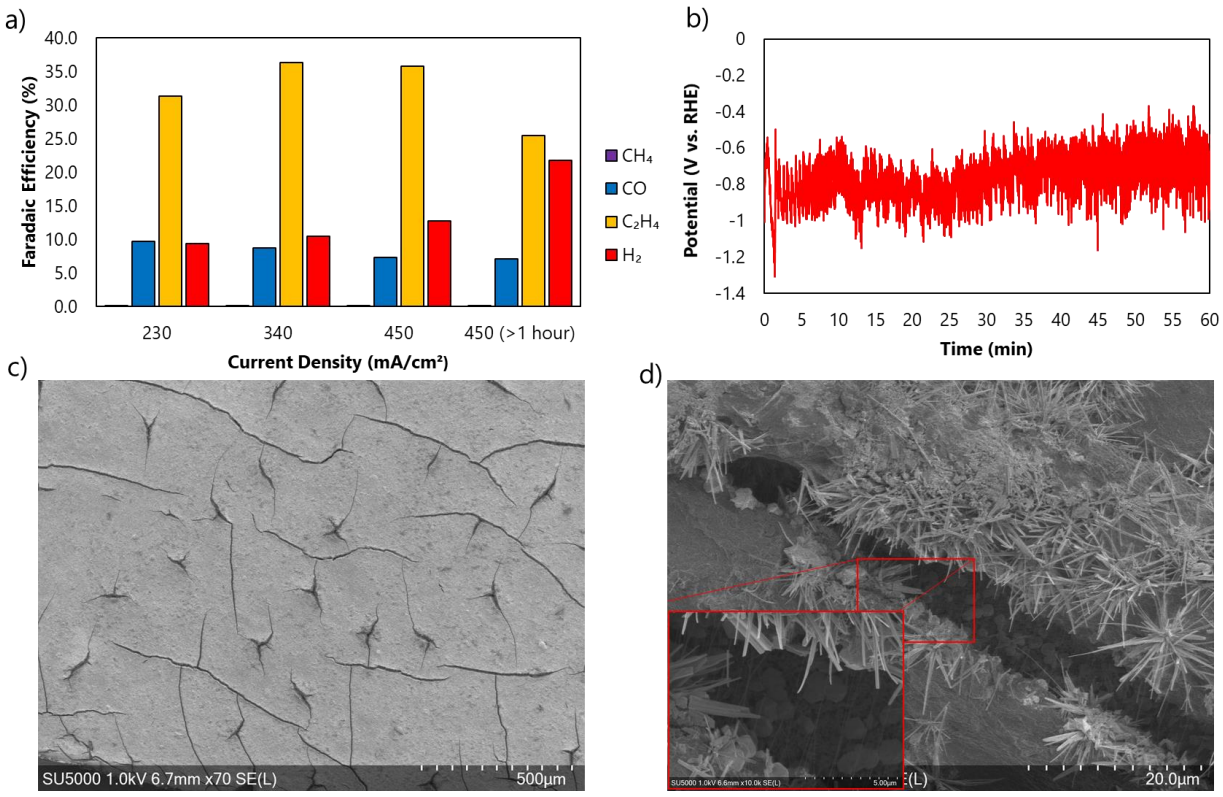

Supplementary Figure 3. (a) Faradaic efficiencies for all major gas products Faradaic efficiencies for all detectable gas products with ERD-Cu in a flowcell configuration. Catalytic runs were performed with constant current. (b) Potential with respect to time for the one hour run at 450 mA/cm^2. (c) SEM image of the cracked catalyst layer on the GDE whereby electrolyte can flood the gas chamber. (d) Zoomed in SEM showing the ERD-Cu nanowhisker morphology growing in the cracks of the catalyst layer.

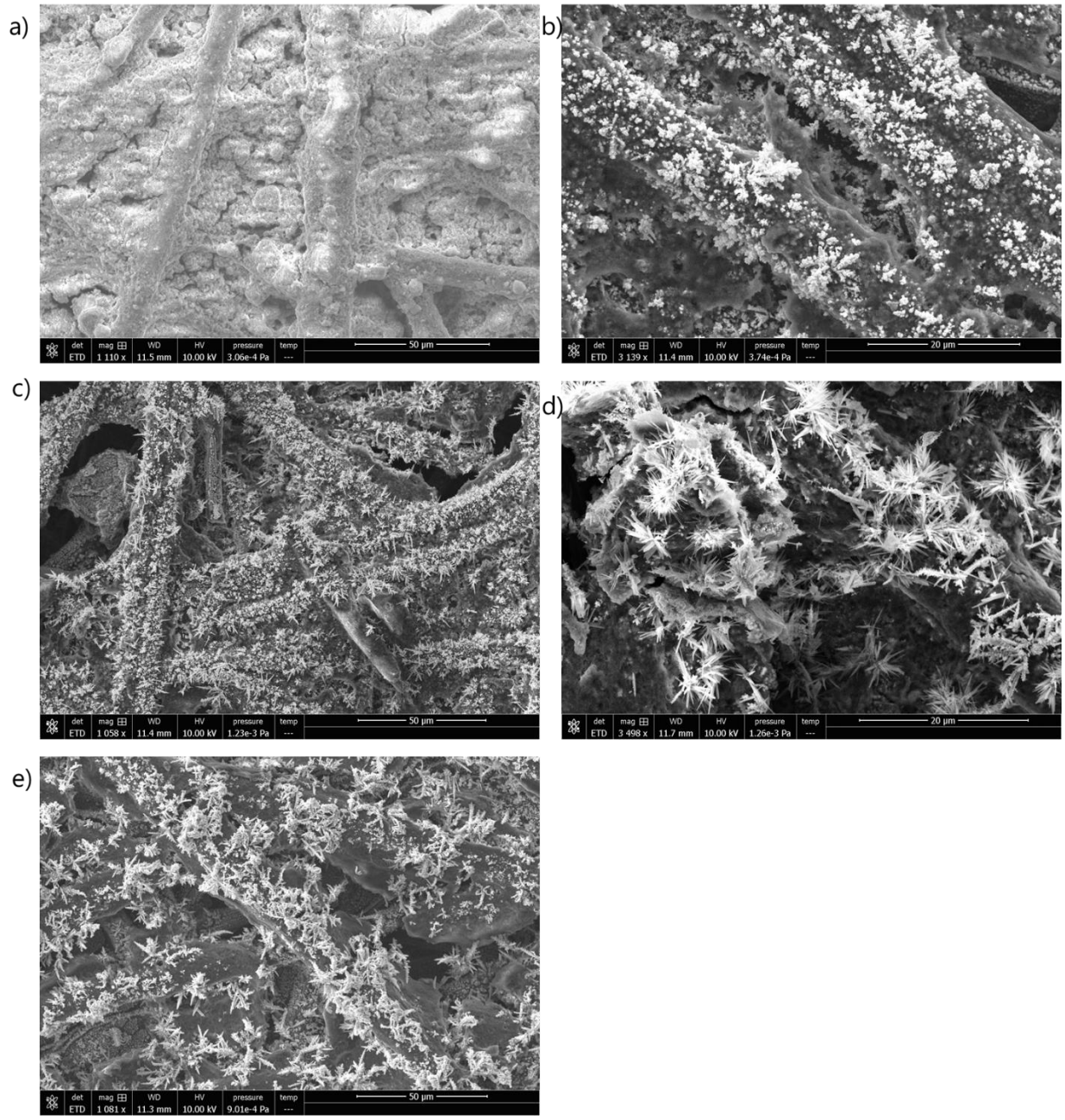

Supplementary Figure 4. SEM images of copper oxychloride sol-gel precursor (a), SGD-Cu formed at (b) -0.7 V vs. RHE, (c) -1.0 V vs. RHE, (d) -1.2 V vs. RHE, (e) -1.4 V vs. RHE showing the homogeneous distribution of nanostructures.

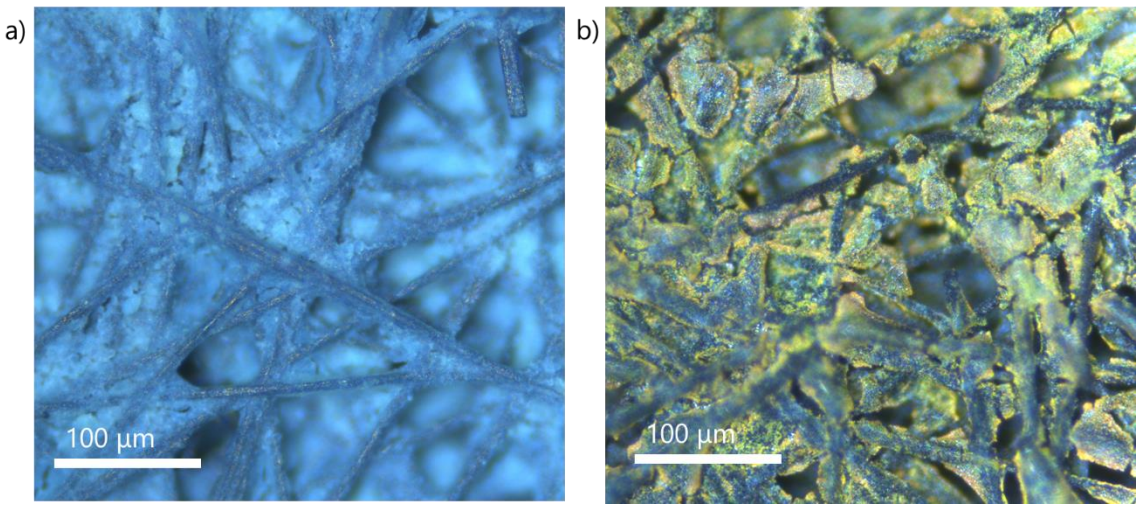

Supplementary Figure 5. Dark-field microscope image of (a) as deposited copper oxychloride sol-gel on carbon paper and (b) SGD-Cu after one hour of reaction under an applied potential of -1.4 V vs. RHE.

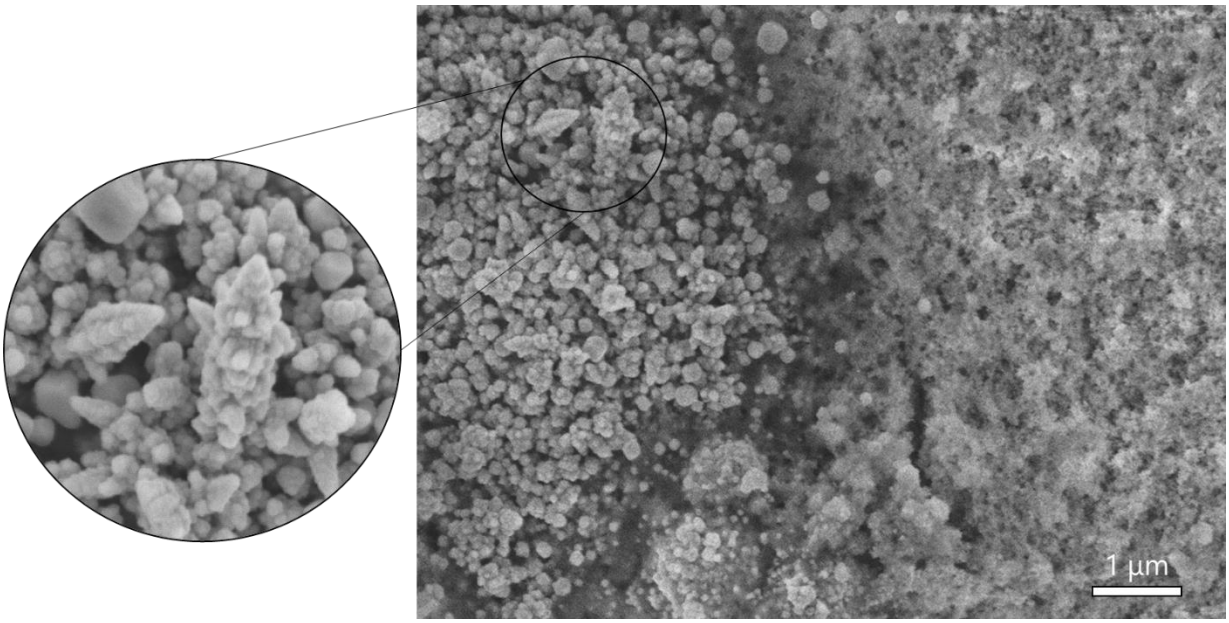

Supplementary Figure 6. SEM images of copper metal growing from the porous copper oxy-chloride sol-gel. Round inset (left) shows a zoomed in image of a copper nanoneedle structure forming.

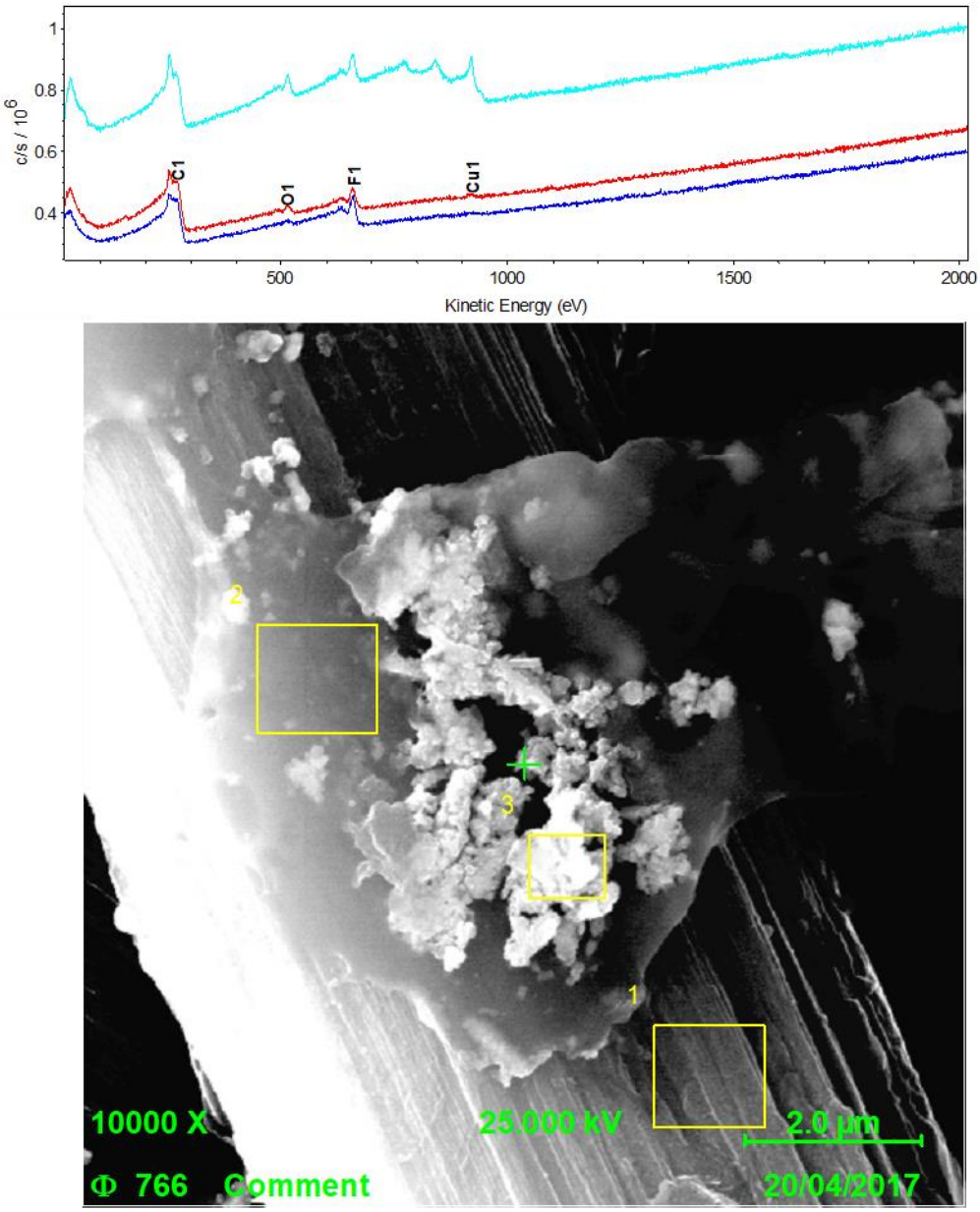

Supplementary Figure 7. Survey Auger spectroscopy scan of different areas on the ERD. Area 1 is the carbon fiber (red), area 2 is the sol-gel matrix primarily copper oxide, and area 3 is the copper nanostructure.

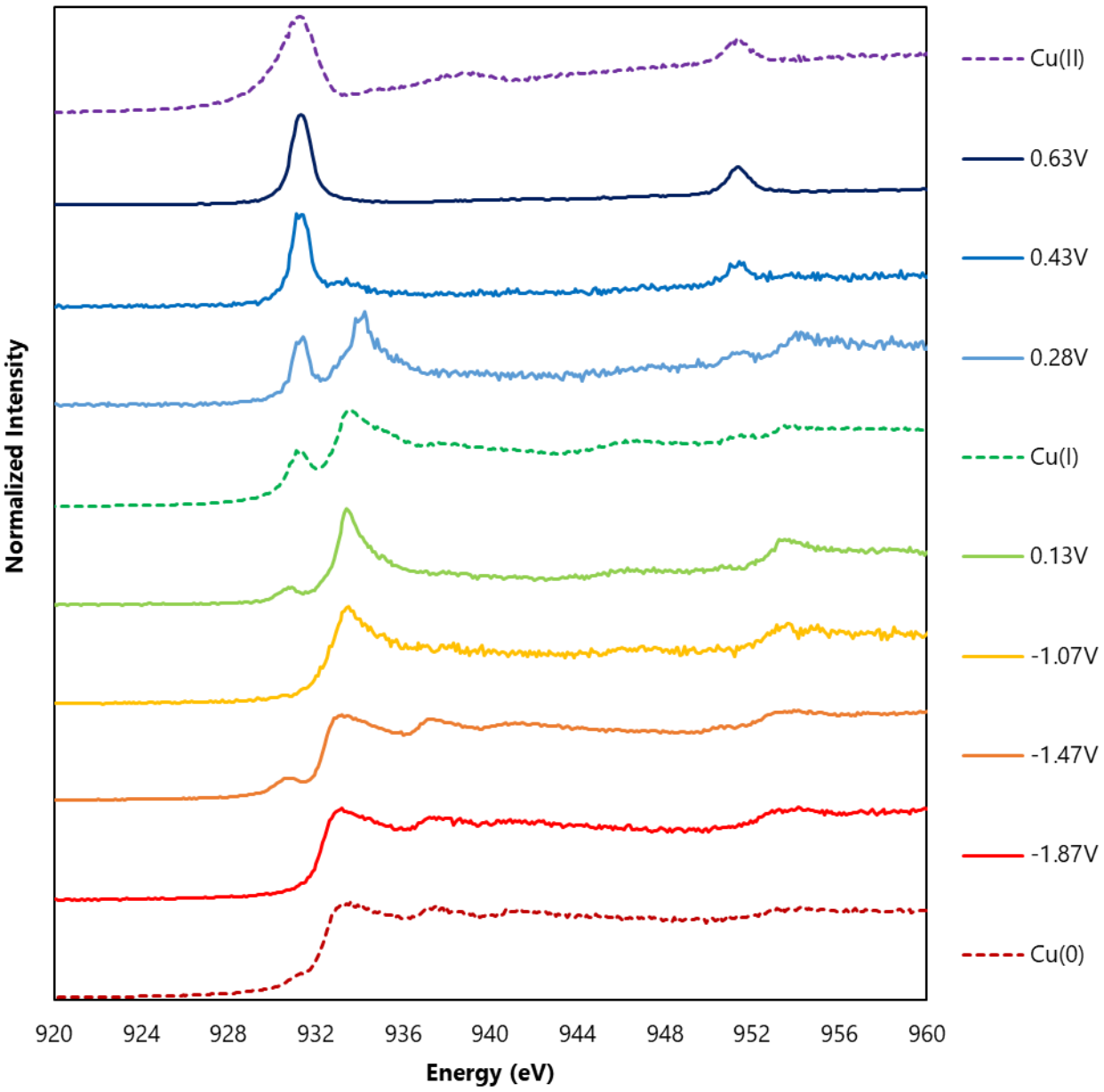

Supplementary Figure 8. *In-situ* sXAS Cu L-edge spectra of SGD-Cu (solid lines) and *ex-situ* spectra of copper standards (dotted lines) from 928 eV to 960 eV clearly showing the L_2 peak.

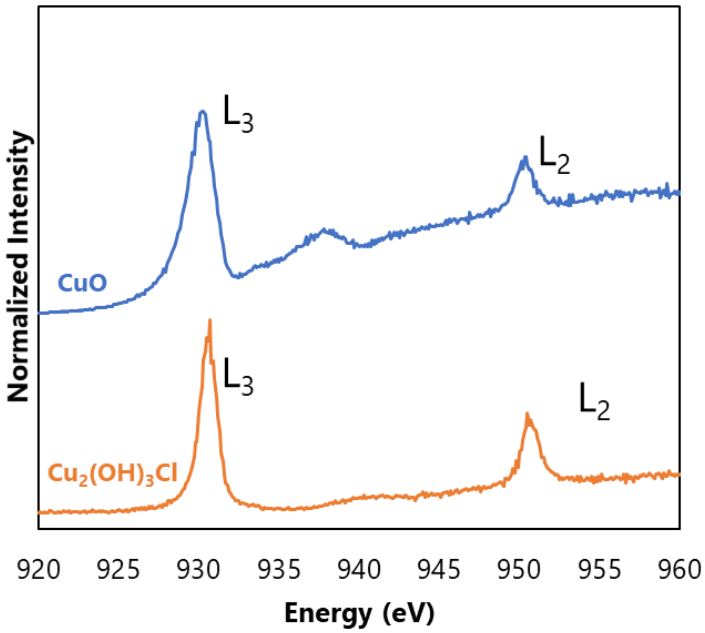

Supplementary Figure 9. sXAS spectra of the Cu L-edge for the copper (II) oxide (blue) control and the copper oxychloride sol-gel (orange).

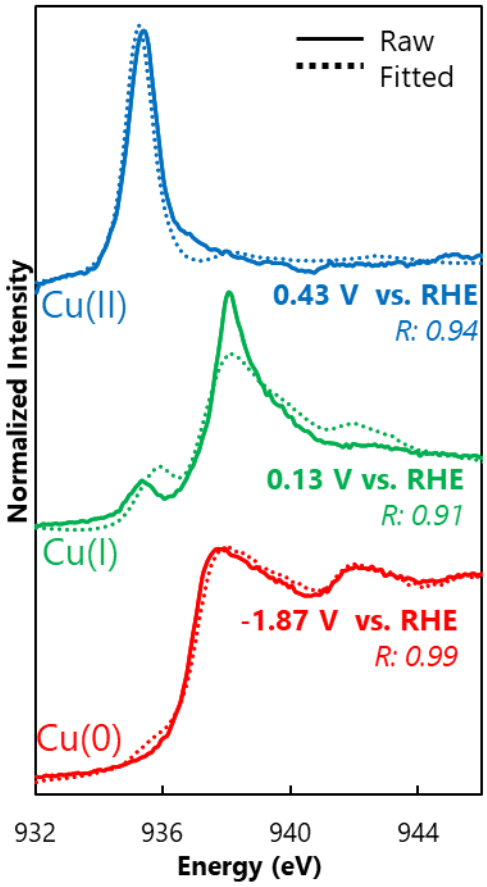

Supplementary Figure 10. Linear combination of Cu, Cu_2O, and CuO spectra as compared to the raw Cu L-edge data of ERD-Cu at 0.43 V vs. RHE (blue), 0.13 V vs. RHE (green), and -1.87 V vs. RHE (red).

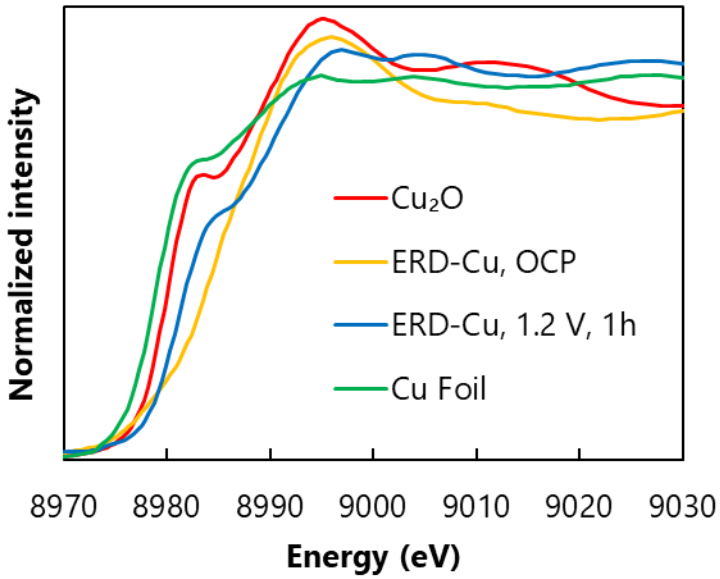

Supplementary Figure 11. *In-situ* Cu K-edge of Cu_2O, Cu foil, and ERD-Cu at OCP and under an applied potential of -1.2 V vs. RHE.

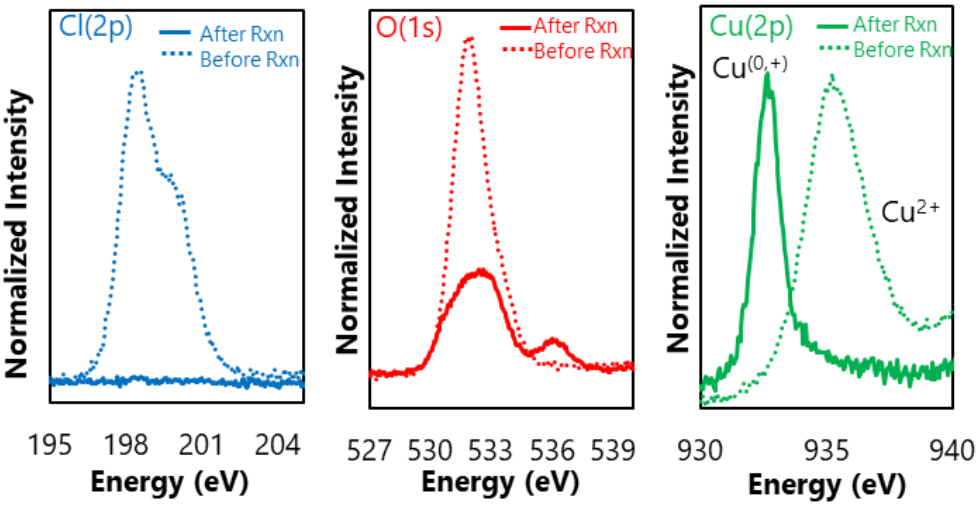

Supplementary Figure 12. XPS spectra of ERD copper before and after reaction.

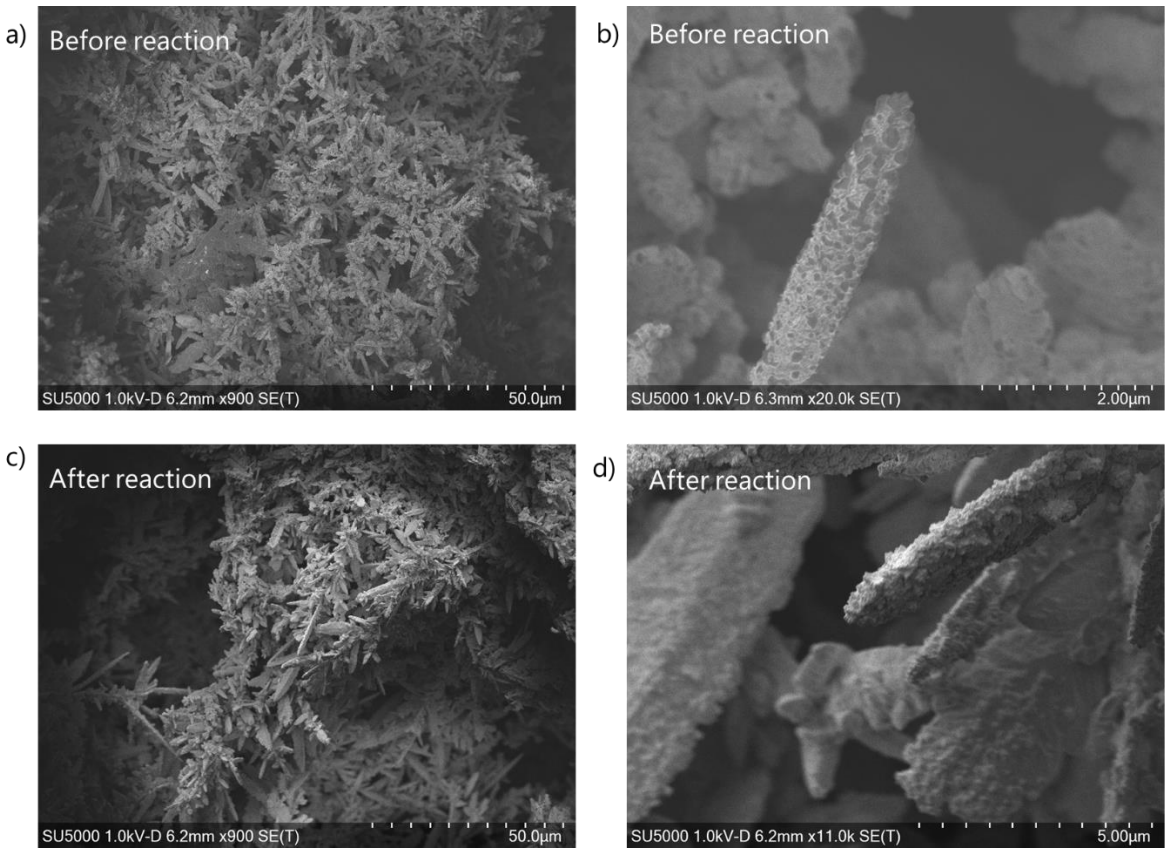

Supplementary Figure 13. Porous copper nanoneedle (NN-Cu) controls before (a,b) and after (c,d) reaction at -1.2 V vs. RHE over at least 1 hour of operation.

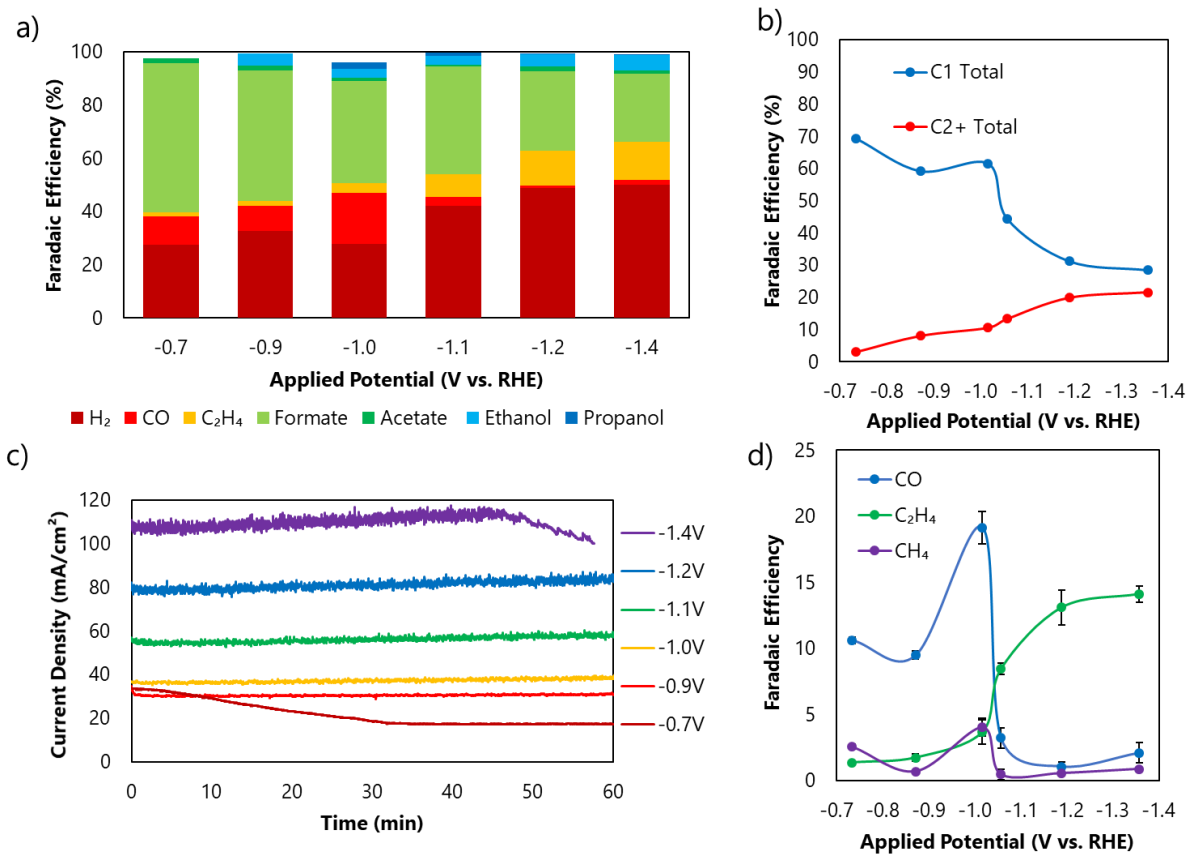

Supplementary Figure 14. (a) Faradaic efficiencies as a function of applied potential for NN-Cu control. (b) The Faradaic efficiencies of C1 vs C2+ products as a function of applied potential. (c) Chronoamperometry plots showing the steady current density of NN-Cu. (d) the Faradaic efficiency of CO2RR gaseous products.

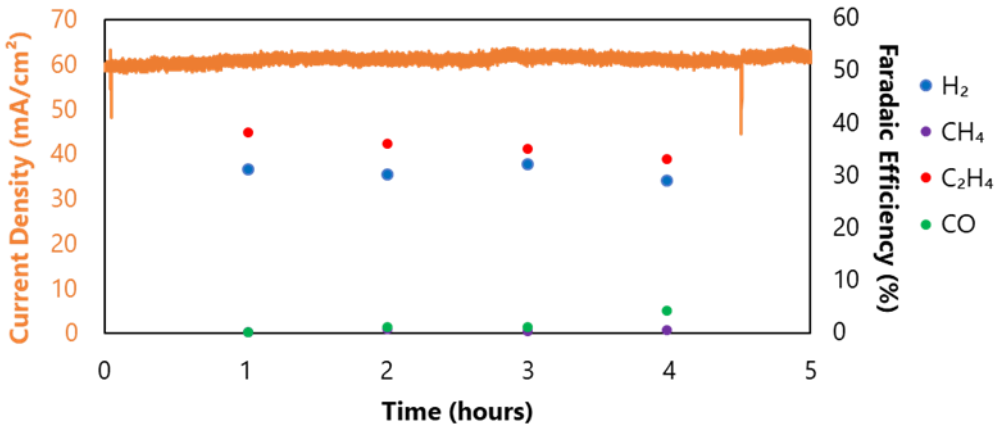

Supplementary Figure 15. Current density (orange) and Faradaic efficiencies of all major gas products of ERD-Cu over 5 hours.

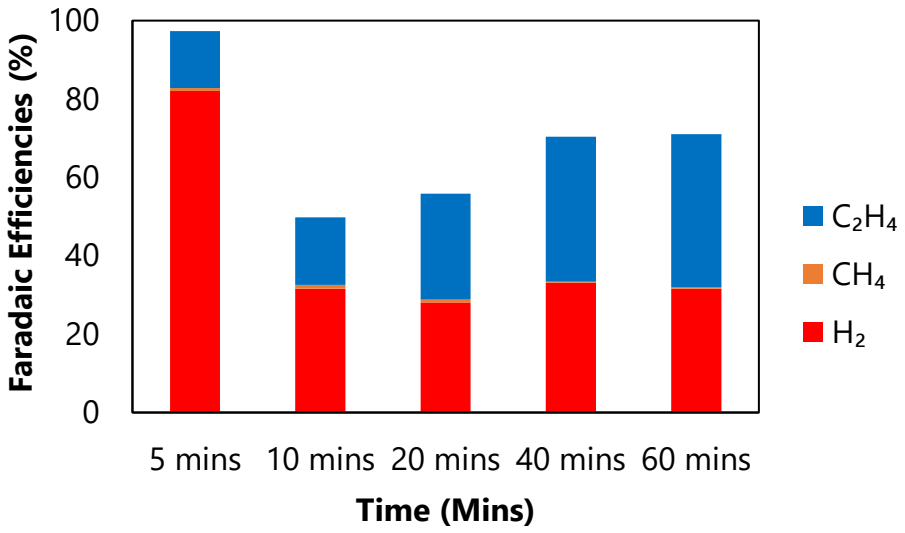

Supplementary Figure 16. The Faradaic efficiencies of all major gas products (H_2, C_2H_4, CH_4) as a function of time within the first hour of ERD-Cu under an applied potential of -1.2 V vs. RHE.

Supplementary Tables

Supplementary Table 1. Faradaic efficiencies and ethylene/methane ratios for copper based catalysts.

Catalyst	Potential (V vs. RHE)	Partial C_2H_4 Current Density (mA/cm2)	C_2H_4 FE (%)	CH_4 FE (%)	C_2H_4/CH_4 ratio
ERD-Cu, H-Cell (this work)	-1.2	22.2	38	0.38	105
ERD-Cu, FlowcelI (this work)		161	35.8	0.18	200
Plasma-Activated Cu[13]	-0.9	7.2	60	4.0	15.0
Cu Nanocubes[14]	-1.1	1.6	41	20.2	2.0
Cu2OCl Nanocubes[15]	-1.6	2.6	22	1.4	15.7
Copper Mesocrystals[16]	-1.0	6.75	27	1.5	18
OD-Cu NPs[17]	-1.1	10.2	34	4.0	8.5
OD-Cu[18]	-1.0	13.3	42	1.0	42
Plasma-Activated Cu Nanocubes[19]	-1.0	15.75	45	3.0	15
Cu(711) Foil[20]	-1.3	2.55	51	3.8	14
Halide-Treated Cu[21]	-1.0	1.04	16	0.3	53
Copper Nanoparticles, Flowcell[10]	-0.8	150	46	1.2	38
Copper Nanodendrites, Flowcell[22]	-2.0	96.9	57	9	6.3

Supplementary Table 2. XRD crystallite size data.

	Cu (111) FWHM	Cu (111) Center	Cu cryst. size	Cu2O (111) FWHM	Cu2O (111) Center	Cu2O cryst. size	CuOHCl (004) FWHM	CuOHCl (004) Center	CuOHCl cryst. size
Before	NA	NA	NA	NA	NA	NA	0.645 °	39.78 °	18 nm
-0.7V	0.33°	43.35 °	45 nm	0.5 °	36.49 °	28 nm	NA	NA	NA
-1.0V	0.3 °	43.38 °	40.7nm	TL	TL	TL	NA	NA	NA
-1.2V	0.39 °	43.36 °	71 nm	0.48 °	36.55 °	27 nm	NA	NA	NA
-1.4V	0.37 °	43.39 °	57 nm	TL	TL	TL	NA	NA	NA

NA – No discernable peak for this species found
TL – Signal for this peak was too weak to acquire reliable data for calculations.

Supplementary Table 3. Cu ratios and R^2 values for the fitting of the linear combination of sXAS spectra.

				Potential (vs. RHE)					
Cu Oxidation State	**1.13**	**0.63**	**0.43**	**0.28**	**0.13**	**-0.27**	**-1.07**	**-1.47**	**-1.87**
Cu(0)	0.00	0.00	0.00	0.01	0.21	0.39	0.46	0.79	1.00
Cu(I)	0.01	0.14	0.43	0.75	0.79	0.61	0.54	0.21	0.00
Cu(II)	0.99	0.86	0.57	0.24	0.00	0.00	0.00	0.00	0.00
R^2 Value	0.967	0.964	0.939	0.906	0.888	0.933	0.982	0.993	0.996
				Time (at -1.2 V vs. RHE)					
Cu Oxidation State	**2 min**	**4 min**	**6 min**	**8 min**	**10 mins**	**1 hour**			
Cu(0)	0.14	0.16	0.18	0.18	0.21	0.77			
Cu(I)	0.84	0.82	0.80	0.80	0.77	0.23			
Cu(II)	0.02	0.02	0.02	0.02	0.02	0.00			
R^2 Value	0.971	0.972	0.969	0.971	0.970	0.936			

Supplementary Table 4. Faradaic efficiencies for ERD-Cu and CuNN catalysts.

ERD-Cu Faradaic Efficiencies (%)									
Potential (V vs. RHE)	**CO**	**H_2**	**CH_4**	**C_2H_4**	**Formate**	**Acetate**	**Ethanol**	**Propanol**	**Total all**
-0.7	19.81	36.03	0.21	2.81	28.50	0.00	0.00	0.00	87.36
-0.9	18.98	24.90	0.20	7.95	25.40	0.50	1.60	0.00	79.52
-1.0	11.08	19.95	0.45	13.04	27.22	1.53	6.27	0.00	79.54
-1.1	6.76	25.29	0.15	15.34	23.90	0.00	12.50	0.00	83.94
-1.2	1.16	31.56	0.03	39.04	16.30	6.70	7.80	0.00	101.28
-1.4	0.00	34.06	0.96	29.41	18.40	0.60	9.70	5.90	99.03
-1.6	0.00	32.67	0.07	27.25	13.30	0.70	13.00	6.50	93.49
CuNN Faradaic Efficiencies (%)									
Potential (V vs. RHE)	**CO**	**H_2**	**CH_4**	**C_2H_4**	**Formate**	**Acetate**	**Ethanol**	**Propanol**	**Total all**
-0.7	10.62	27.59	2.55	1.36	56.15	1.74	0.00	0.00	100.44
-0.9	9.48	32.74	0.68	1.73	48.99	1.81	4.58	0.00	100.35
-1.0	19.16	27.89	4.02	3.66	38.28	1.34	3.25	2.39	101.92
-1.1	3.22	42.27	0.44	8.45	40.70	0.38	3.31	1.23	101.19
-1.2	1.05	48.84	0.54	13.10	29.67	1.91	4.40	0.48	100.39
-1.4	2.09	49.94	0.87	14.12	25.52	1.28	5.92	0.27	100.87
-1.6	1.52	52.32	0.31	14.89	23.89	2.20	4.01	0.86	100.44

Supplementary Table 5. Thermodynamic quantities used in the DFT calculations

Cu(111)					
Adsorbates	E_elec	ZPE	∫CvdT	(-TΔS)	G
slab	-164.52				
CO	-179.92	0.19	0.08	-0.19	-179.84
COCO	-195.33	0.39	0.15	-0.35	-195.14
COH	-182.49	0.47	0.09	-0.20	-182.13
OCCOH	-197.68	0.72	0.14	-0.32	-197.14
Cu(211)					
Adsorbates	E_elec	ZPE	∫CvdT	(-TΔS)	G
slab	-244.63				
CO	-260.34	0.21	0.06	-0.10	-260.16
COCO	-275.79	0.37	0.16	-0.34	-275.60
COH	-261.49	0.45	0.09	-0.18	-261.13
OCCOH	-277.75	0.72	0.13	-0.28	-277.18
ERD-Cu(111)					
Adsorbates	E_elec	ZPE	∫CvdT	(-TΔS)	G
slab	-257.72				
CO	-274.56	0.21	0.06	-0.11	-274.39
COCO	-290.25	0.42	0.13	-0.23	-289.93
COH	-276.19	0.51	0.07	-0.14	-275.76
OCCOH	-292.20	0.72	0.13	-0.29	-291.63
ERD-Cu(211)					
Adsorbates	E_elec	ZPE	∫CvdT	(-TΔS)	G
slab	-267.14				
CO	-283.43	0.19	0.08	-0.19	-283.35
COCO	-298.70	0.40	0.14	-0.28	-298.44
COH	-285.92	0.49	0.08	-0.16	-285.52
OCCOH	-301.31	0.71	0.14	-0.32	-300.78

Supplementary Table 6. Gibbs energy of formation for reaction intermediates and CO binding energies.

Catalyst	**G_{form}COH* (eV)**	**G_{form}OCCOH* (eV)**	**CO $E_{binding}$ (eV)**
Cu(111)	1.176	1.461	-0.1
Cu(211)	2.502	1.89	-0.3
ERD-Cu(111)	2.105	1.772	-1.0
ERD-Cu(211)	1.306	1.129	-1.5

Supplementary References

1. Hafner, J. Ab-initio simulations of materials using VASP: Density-functional theory and beyond. *Journal of Computational Chemistry* **29,** 2044–2078 (2008).

2. Blöchl, P. E. Projector augmented-wave method. *Phys. Rev. B* **50,** 17953–17979 (1994).

3. Perdew, J. P., Burke, K. & Ernzerhof, M. Generalized Gradient Approximation Made Simple. *Phys. Rev. Lett.* **77,** 3865–3868 (1996).

4. Kresse, G. From ultrasoft pseudopotentials to the projector augmented-wave method. *Phys. Rev. B* **59,** 1758–1775 (1999).

5. Monkhorst, H. J. & Pack, J. D. Special points for Brillouin-zone integrations. *Phys. Rev. B* **13,** 5188–5192 (1976).

6. Head, J. & Zerner, M. A Broyden-Fletcher-Goldfarb-Shanno Optimization Procedure for Molecular Geometries. *Chem. Phys. Lett.* **122,** 264–270 (1985).

7. Hjorth Larsen, A. *et al.* The atomic simulation environment—a Python library for working with atoms. *J. Phys. Condens. Matter* **29,** 273002 (2017).

8. Peterson, A. a., Abild-Pedersen, F., Studt, F., Rossmeisl, J. & Nørskov, J. K. How copper catalyzes the electroreduction of carbon dioxide into hydrocarbon fuels. *Energy Environ. Sci.* **3,** 1311 (2010).

9. Xiao, H., Goddard, W. A., Cheng, T. & Liu, Y. Cu metal embedded in oxidized matrix catalyst to promote CO2 activation and CO dimerization for electrochemical reduction of CO2. *Proc. Natl. Acad. Sci. U. S. A.* **114,** 6685–6688 (2017).

10. Ma, S. *et al.* One-step electrosynthesis of ethylene and ethanol from CO2 in an alkaline electrolyzer. *J. Power Sources* **301,** 219–228 (2016).

11. Nørskov, J. K., Abild-Pedersen, F., Studt, F. & Bligaard, T. Density functional theory in surface chemistry and catalysis. *Proc. Natl. Acad. Sci. U. S. A.* **108,** 937–43 (2011).

12. de Groot, F. M. F. *et al.* 1s2p resonant inelastic X-ray scattering of iron oxides. *J. Phys. Chem. B* **109,** 20751–62 (2005).

13. Mistry, H. *et al.* Highly selective plasma-activated copper catalysts for carbon dioxide reduction

to ethylene. *Nat. Commun.* **7,** 12123 (2016).

14. Loiudice, A. *et al.* Tailoring Copper Nanocrystals towards C $_2$ Products in Electrochemical CO $_2$ Reduction. *Angew. Chemie Int. Ed.* **55,** 5789–5792 (2016).

15. Lee, S., Kim, D. & Lee, J. Electrocatalytic Production of C3-C4 Compounds by Conversion of CO $_2$ on a Chloride-Induced Bi-Phasic Cu $_2$ O-Cu Catalyst. *Angew. Chemie Int. Ed.* **54,** 14701–14705 (2015).

16. Chen, C. S. *et al.* Stable and selective electrochemical reduction of carbon dioxide to ethylene on copper mesocrystals. *Catal. Sci. Technol.* **5,** 161–168 (2015).

17. Kas, R. *et al.* Electrochemical CO2 reduction on Cu2O-derived copper nanoparticles: controlling the catalytic selectivity of hydrocarbons. *Phys. Chem. Chem. Phys.* **16,** 12194 (2014).

18. Handoko, A. D. *et al.* Mechanistic Insights into the Selective Electroreduction of Carbon Dioxide to Ethylene on Cu $_2$ O-Derived Copper Catalysts. *J. Phys. Chem. C* **120,** 20058–20067 (2016).

19. Gao, D. *et al.* Plasma-Activated Copper Nanocube Catalysts for Efficient Carbon Dioxide Electroreduction to Hydrocarbons and Alcohols. *ACS Nano* **11,** 4825–4831 (2017).

20. Hori, Y., Takahashi, I., Koga, O. & Hoshi, N. Selective Formation of C2 Compounds from Electrochemical Reduction of CO $_2$ at a Series of Copper Single Crystal Electrodes. *J. Phys. Chem. B* **106,** 15–17 (2002).

21. Kwon, Y., Lum, Y., Clark, E. L., Ager, J. W. & Bell, A. T. CO $_2$ Electroreduction with Enhanced Ethylene and Ethanol Selectivity by Nanostructuring Polycrystalline Copper. *ChemElectroChem* **3,** 1012–1019 (2016).

22. Reller, C. *et al.* Selective Electroreduction of CO 2 toward Ethylene on Nano Dendritic Copper Catalysts at High Current Density. *Adv. Energy Mater.* **7,** 1602114 (2017).